ceramics

MDPI

Article

Influence of Isovalent 'W' Substitutions on the Structure and Electrical Properties of $La_2Mo_2O_9$ Electrolyte for Intermediate-Temperature Solid Oxide Fuel Cells

Tanmoy Paul *,† and Yoed Tsur

Department of Chemical Engineering and the Grand Technion Energy Program, Technion-Israel Institute of Technology, Haifa 3200003, Israel; tsur@technion.ac.il

* Correspondence: paultanmoy00@gmail.com

† Present address: Department of Condensed Matter Physics and Materials Science, S. N. Bose National Centre for Basic Sciences, Kolkata 700098, India.

Abstract: Lanthanum molybdenum oxide ($La_2Mo_2O_9$, LAMOX)-based ion conductors have been used as potential electrolytes for solid oxide fuel cells. The parent compound $La_2Mo_2O_9$ undergoes a structural phase transition from monoclinic ($P2_1$) to cubic ($P2_13$) at 580 °C, with an enhancement in oxide ion conductivity. The cubic phase is of interest because it is beneficial for oxide ion conduction. In search of alternative candidates with a similar structure that might have a stable cubic phase at lower temperatures, we have studied the variations of the crystal structure and ionic conductivity for 25, 50, 62.5 and 75 mol% W substitutions at the Mo site using high-temperature X-ray diffraction, dilatometry, and impedance spectroscopy. Highly dense ceramic samples have been synthesized by solid-state reaction in a two-step sintering process. Low-angle X-ray diffraction and Rietveld refinement confirm the stabilization of the cubic phase for all compounds in the entire temperature range considered. The substitutions of W at the Mo site produce a decrement in the lattice parameter. The thermal expansion coefficients in the high-temperature range of the W-substituted ceramics, as determined by dilatometry, are much higher than that of the unmodified sample. The impedance spectra have been modeled using a modified genetic algorithm within 300–600 °C. A distribution function of the relaxation times is obtained, and the contributions of ohmic drop, grains and grain boundaries to the conductivity have been identified. Overall, our investigation provides information about cationic substitution and insights into the understanding of oxide ion conductivity in LAMOX-based compounds for developing solid oxide fuel cells.

Keywords: oxide ion conductor; W-substitution; crystal structure; grain boundary; impedance spectroscopy; DFRT

Citation: Paul, T.; Tsur, Y. Influence of Isovalent 'W' Substitutions on the Structure and Electrical Properties of $La_2Mo_2O_9$ Electrolyte for Intermediate-Temperature Solid Oxide Fuel Cells. *Ceramics* **2021**, *4*, 502–515. https://doi.org/10.3390/ceramics4030037

Academic Editors: Giuseppe Viola and Gilbert Fantozzi

Received: 10 August 2021
Accepted: 14 September 2021
Published: 16 September 2021

1. Introduction

Yttria-stabilized zirconia is a widely studied oxide ion conductor used as a solid oxide fuel cell electrolyte. In spite of its high chemical and thermal stability, the oxide ion conductivity is insufficient below 800 °C for use in intermediate-temperature solid oxide fuel cells. Among alternative oxide materials, $La_2Mo_2O_9$ [1–4] provides high ionic conductivity in comparison with $LaGaO_3$-based perovskites, CeO_2-based fluorite type structure, and apatites from $La_{10-x}Si_6O_{26\pm\delta}$. Indeed, in the case of $La_2Mo_2O_9$, high oxide ion conductivity is observed after a structural phase transition from room-temperature monoclinic (α) to high-temperature cubic (β) at 580 °C [5]. A series of reports have been published regarding the quest to stabilize the β form down toward room temperature by substituting alkali, alkaline and rare earth cations in both the La and Mo sites [6–17].

In addition to stabilizing the cubic phase, the substitution of Mo^{+6} by W^{+6} extends the material's redox stability range with a high ion transport number at an oxygen partial pressure of 10^{-15} atm [5,18,19]. Fortunately, W-substituted $La_2Mo_2O_9$ could be used as

a solid oxide fuel cell (SOFC) electrolyte in a reducing atmosphere and at intermediate temperatures of operation [2]. The effect of W substitution shows a cubic phase with an abrupt decrease in cell parameter above W:Mo = 1 that has been reported and attributed to a possible change in the coordination number of the hexavalent ions [20]. This deviation was studied using ab initio calculations, which suggested that it is due to a nonlinear change in Mo/W-O bond lengths with W content [21]. Again, a slight deviation from cubic symmetry is noted for a W content of less than 0.25 in $La_2Mo_{2-x}W_xO_9$ [22]. The effect of oxygen partial pressure on ionic conductivity is studied in oxygen, air, argon and CO-CO_2 mixtures [23]. Interestingly, the presence of W stabilizes the reduction of Mo^{+6} [23,24]. Apart from oxide ion conductivity, n-type electronic conductivity arises due to the mixed-valence states of Mo, which is reduced as the W content increases [2].

The structural and oxide ion conductivity studies, both in air and a reducing atmosphere, were investigated for co-substituted samples. For instance, $La_{1.8}Dy_{0.2}Mo_{2-x}W_xO_9$ possesses a cubic structure along with the anomaly in cell volume [25], as reported earlier for W substitution only. A cubic phase is also reported for $(La_{1-x}Sr_x)_2Mo_{1.5}W_{0.5}O_{9-\delta}$ at room temperature [26] and $La_{1.9}Ba_{0.1}Mo_{2-x}W_xO_{8.95}$ ($0 \leq x \leq 0.40$) [27]. An Arrhenius to Vogel–Tammann–Fulcher (VTF)-type transition in oxide ion conductivity is observed for $La_2Mo_{2-x}W_xO_9$ ($x \leq 1.4$) and co-substituted samples [28]. Such a deviation in oxide ion conductivity is a characteristic feature in several ionic conductors. It might be interesting to study such puzzling behavior from the point of view of ion transport, coupled with structural stability.

To obtain further insights into the conduction mechanisms in this article, we have re-investigated the crystal structure with a high-temperature, high-resolution X-ray diffraction technique and dilatometry, and studied the electrical properties by impedance spectroscopy. The impedance response has been studied using the distribution function of relaxation times (DFRTs), which has not been previously discussed for W-substituted $La_2Mo_2O_9$ solid solutions. The W substitutions show an anomaly in lattice parameters, as determined by high-temperature X-ray diffraction. The dilatometry and X-ray diffraction show the stabilization of the cubic phase in the entire temperature range. Furthermore, we have identified a transition in thermal expansion curves for the W-substituted samples that is composition-dependent. The ac impedance measurements, coupled with DFRTs, identifies the effect of grain and grain boundaries in compositions up to W:Mo = 3 (x = 1.5, $La_2Mo_{2-x}W_xO_9$), analyzing the complicated impedance spectra obtained between 300 and 600 °C. Apart from grain and grain boundaries effects, the shift in DFRT peaks also marks the thermally activated Arrhenius to VTF transitions. The annihilation of the DFRT peak related to the grain effect is also related to the distribution of grain sizes.

2. Materials and Methods

Ceramic samples of compositions comprising $La_2Mo_{2-x}W_xO_9$ ($0.50 \leq x \leq 1.5$) (henceforth 0.5 W, 1.0 W, 1.25 W and 1.5 W) were prepared, using a high-temperature solid-state reaction method. Stoichiometric amounts of La_2O_3 (Aldrich, 99.9%, Saint Louis, MO, USA), MoO_3 (Strem Puratrem, 99.999%, Newburyport, MA, USA) and WO_3 (Aldrich, 99.9%, MO, USA) were mixed thoroughly in ethanol in a homogenizer. The dried mixtures were heated in an alumina crucible in a furnace for 12 h at 500 °C. After cooling, the calcined mixtures were ground and sintered at 1000–1200 °C for 12 h in air. Finally, the fine powders were pressed into pellets of 10 mm diameter and 1–2 mm thickness via isostatic pressing at 300 MPa for 1 min. The maximum temperatures were maintained at 1200 °C, depending on the W content, with cooling at a rate of 5 °C/min.

The phase purity was checked by room temperature and high-temperature X-ray diffraction on an X-ray diffractometer (Rigaku Smartlab 9 kW) using the Bragg–Brentano mode, CuKα radiation, 45 kV and 150 mA. High-temperature diffraction patterns were collected in air up to 900 °C in the range of 15–90°, with a step size of 0.02° and 1.5 s/step in a graphite dome with an Anton Paar, TCU200 controller, Graz, Austia. All the X-ray diffraction patterns were recorded on pellets. The Rietveld refinement was performed using

FullProf [29] for full-pattern matching. The microstructures and grain size were analyzed using a scanning electron microscope (Zeiss, Ultra-Plus, Jena, Germany). The density of the pellets was measured by Archimedes principle, using ethanol as immersing medium, to be greater than 90% of their theoretical densities. The dilatometric measurements were performed in a dilatometer (Netzsch, DIL 402 L, Baiuvarii, Germany) from room temperature to 900 °C at a heating rate of 5 °C/min, in a 10% H_2-N_2 gas mixture.

The complex impedance measurements of the ceramic pellets were measured in air in the frequency range of 1 MHz–0.01 Hz at different temperatures. Pt paste was painted on both faces of the pellets and cured at first at 300 °C for 30 min and then at 900 °C for 1 h. The measurements were performed at open-circuit potential with an AC voltage of 50 mV in an impedance analyzer (Biologic, Model VSP, Pariset, France) after a temperature stabilization of 30 min.

The DFRT for all the samples at different temperatures was found by impedance spectroscopy genetic programming (ISGP) [30–38], a MATLAB-based open-source code. The following equation shows the correlation between the measured impedance and the DFRT:

$$Z(\omega) = R_{\infty} + R_{pol} \int_{-\infty}^{+\infty} \frac{\Gamma(\log(\tau))}{1 + i\omega\tau} \mathrm{d}(\log(\tau)) \quad (1)$$

where Z is the impedance, R_{∞} is the series resistance, R_{pol} is the total polarization resistance, Γ is the DFRT, τ is the relaxation time and ω is the angular frequency. In general, a DFRT consists of several peaks, and each peak corresponds to a particular relaxation process, distinguished by a time constant (τ_p). A discrepancy–complexity plot was employed to monitor the progress during computation. Each run is repeated two times automatically under the same conditions, to ensure that the results are not at a local minimum. A detailed description of the error values in DFRTs can be found in [39]. Before each run, the integrity of the impedance data is checked with the Kramers–Krönig relations, as an integral part of the ISGP code. A typical impedance plot is shown in Figure S1, justifying the data as being appropriate for evaluation.

The DFRT approach is superior to conventional equivalent circuit modeling as the latter suffers from non-uniqueness, overfitting, sometimes missing bandwidths and also more presumptions. The peak position, and its shift due to temperature variation, are identified by the DFRT model and the method is robust and accurate. Secondly, the R_{eff} and C_{eff} are computed by ISGP, which helps to identify the true capacitance. On the other hand, conventional equivalent circuit modeling provides the constant phase element (Q) in lieu of true capacitance.

3. Results and Discussion

3.1. X-ray Diffraction

Room-temperature XRD patterns for different W-substituted samples and undoped α-$La_2Mo_2O_9$ are shown in Figures 1 and S2, respectively. The sharp and well-defined Bragg peaks indicate the high quality of the crystallinity. Interestingly, both undoped and doped samples contain the same number of peaks, irrespective of their structural phases (Figures 1 and S2). The agreement factors (Table S1), obtained after the Rietveld refinement in Figure S2b, suggest a monoclinic phase for undoped $La_2Mo_2O_9$. The Rietveld refinement of the patterns confirms the cubic phase (space group $P2_13$) for all the W-substituted samples, in agreement with ICSD card no. 172611. A polynomial function with 6 coefficients was used to set the background and a pseudo-Voigt shape function was used for profile-matching, with a variation in scale factors and zero shift. Finally, the cell parameters, atomic coordinates and occupancies of the cations were varied. The agreement factors of the refinement are presented in Table S1. The refinement results indicate that, at room temperature, the cell parameter of the 0.5 W sample is 7.1542 (4) Å, which is higher than undoped β-$La_2Mo_2O_9$ (7.1490 Å). Overall, the cell parameters do not vary much (0.0052 Å). This is because the radius of W^{+6} (0.42 and 0.60 Å in CN4 and CN6 respectively) is similar to that of Mo^{+6} (0.41 and 0.59 Å in CN4 and CN6 respectively) [40]. This result

is consistent with the previous studies [20]. The theoretical densities, as deduced from the Rietveld refinement, are in good agreement with that determined by the Archimedes principle (Table 1).

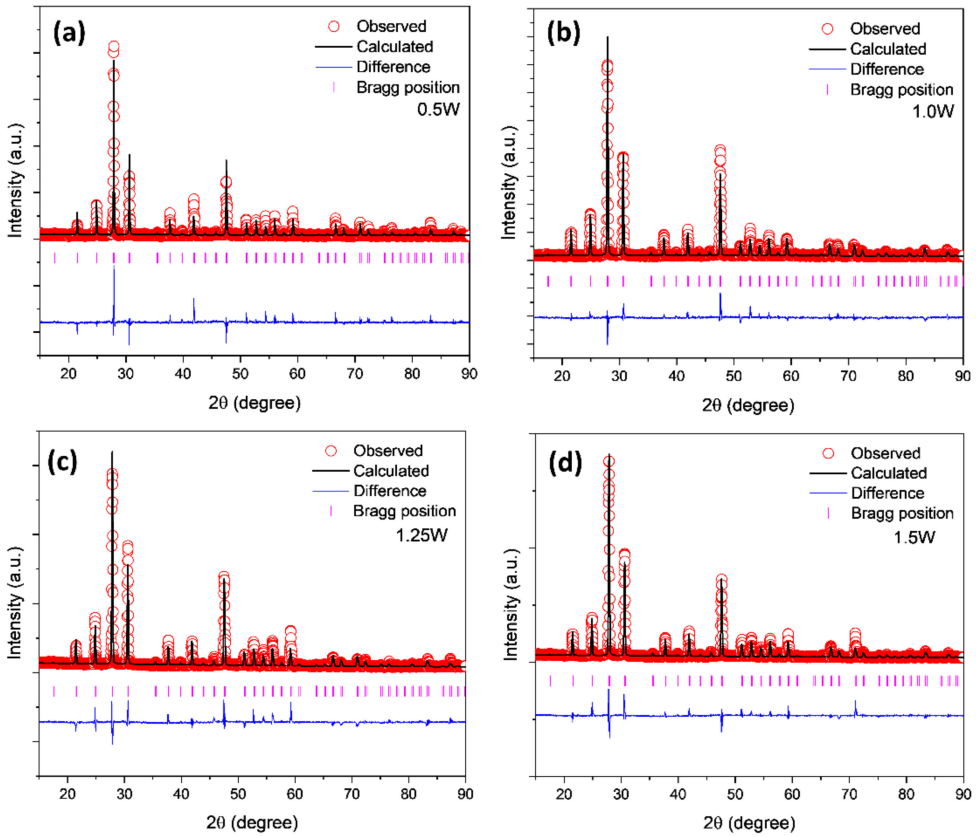

Figure 1. Rietveld refinement patterns for different W-doped samples at room temperature; (**a**) 0.50 W; (**b**) 1.0 W; (**c**) 1.25 W; (**d**) 1.5 W.

Table 1. Experimental and theoretical densities, as determined by Rietveld refinement, for different W-substituted samples. The grain size variation is also shown for different W-substituted samples.

Composition (x)	Experimental Density (g cm^{-3})	Theoretical Density (g cm^{-3})	Grain Size (μm)
0	5.498	5.561	12 [1]
0.5	5.547	6.739	7.9
1.0	6.344	6.759	7.06
1.25	6.508	6.751	7.45
1.50	6.821	6.769	7.16

[1] From [41].

Figure 2a shows the unit cell parameter evolution upon heating, as obtained from the refinements. The composition dependence of the cell parameter in Figure 2b shows a non-linear variation, in agreement with previous studies [20]. One possible reason is the decrement in the coordination numbers of W upon substitution, as well as the non-linear evolution of [O1La_3(Mo,W)] antitetrahedral units [20,21]. Here O1 is an oxygen lattice site.

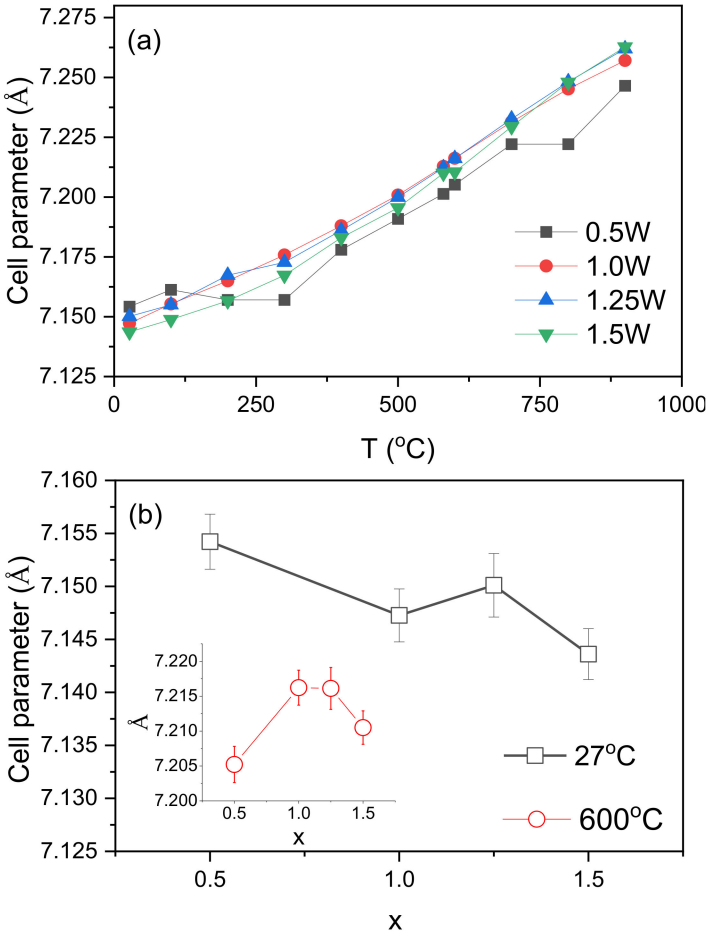

Figure 2. (**a**) Variation of unit-cell parameters at different temperatures for different W-substituted samples. (**b**) Composition dependence of unit-cell parameters at two temperatures. The solid lines are guides to the eye.

3.2. Dilatometry

Dilatometric studies on the W-substituted samples show a smooth expansion profile, as opposed to the irregular profile for $La_2Mo_2O_9$ (Figure 3). The average thermal expansion coefficients (TEC) are found to be higher in the high-temperature regime than that at the low-temperature regime (Table 2). These TECs are found to be higher than other SOFC candidate materials. Two TECs can be identified, due to two linear regimes, as observed by comparing the dashed lines for all the W-substituted samples. A similar finding was reported by Marrero-Lopez et al. [18] with the transition at 550 °C, as shown in Table 2. We did not see a kink at around 580 °C as is seen in undoped $La_2Mo_2O_9$; thus, the transition does not reflect a structural phase transition for the doped samples. It is worth noting that in the undoped $La_2Mo_2O_9$, an $\alpha \leftrightarrow \beta$ phase transition is observed in the thermal expansion curve around 580 °C (Figure 3a). However, with increasing temperature, a "chemical" contribution could increase the thermochemical expansion as a result of oxygen loss from the lattice. A similar nonlinearity in dilatometric curves is also reported, e.g., for Mn-substituted 5 mol% YSZ oxide ion conductors [42] and gadolinia-doped ceria (Baral and Tsur, to be published). Furthermore, the anomaly in conductivity (see later section) around 450 °C for W-substituted samples could be related to thermochemical expansion, as observed in the dilatometry curves.

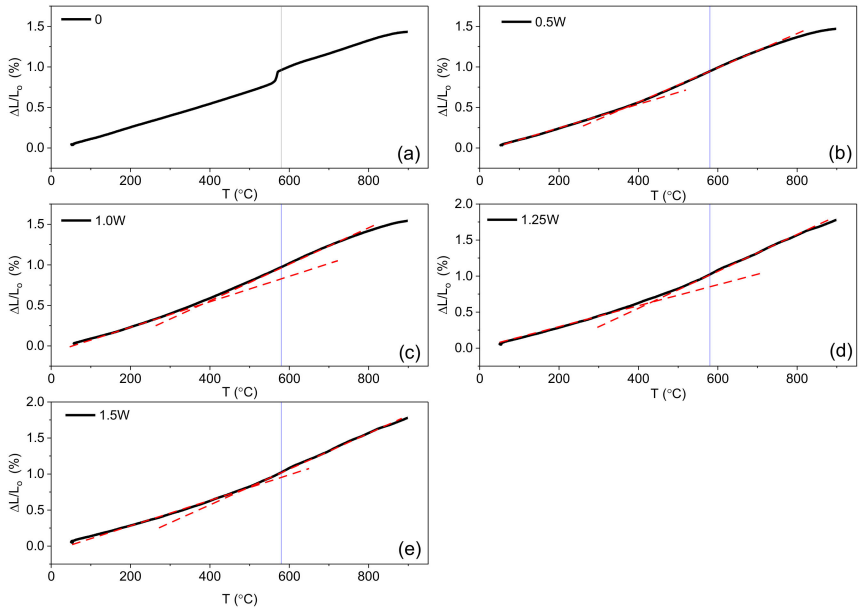

Figure 3. Variation of thermal expansion for different samples; (**a**) undoped $La_2Mo_2O_9$, (**b**) 0.50 W; (**c**) 1.0 W; (**d**) 1.25 W; (**e**) 1.5 W. The vertical lines at 580 °C represent the phase transition of undoped $La_2Mo_2O_9$. The dashed lines indicate the linear regimes.

Table 2. Thermal expansion coefficient for different W-substituted samples at different temperature regimes. The TEC, as obtained from the literature, is also shown. '-' represents unavailable values in literature.

Composition	From Figure 4		From Ref. [18]	
(x)	T (°C)	TEC × 10^{-6} ($°C^{-1}$)	T (°C)	TEC × 10^{-6} ($°C^{-1}$)
0	100–520	14.7	25–550	13.5
	600–795	15.8	625–800	16.8
0.5	110–365	15.3	25–450	15.2
	490–710	21.6	550–800	19.9
1.0	57–317	15.3	25–500	15.4
	350–765	21.4	550–800	20.7
1.25	70–445	16.5	-	-
	550–870	24.3	-	-
1.50	90–400	16.5	25–500	13.9
	600–895	23.2	550–800	21.0

3.3. Microstructure

The microstructure of all the W-substituted samples is shown in Figure 4. The samples have low porosity, with a relative density of >90%, and have well-connected grains. From the porosity measurements using SEM micrographs, it is ascertained that 0.5 W, 1.0 W and 1.5 W samples have a porosity of ~1%, whereas the 1.25 W sample has a porosity of ~3.5%, which apparently contradicts the density measurements. However, our thorough SEM studies (Figure S3) suggest that the depth of the pores is within the surface only, without affecting the pellet density. The grain size of all the W-substituted samples shows only a little effect from W substitution (see Table 1, Figures 4 and S4). The average grain size is ~8 μm, which is much lower than that of undoped $La_2Mo_2O_9$. The average grain size for $La_2Mo_2O_9$ pellet, as sintered at 800 °C, is ~12 μm [41]. Note that $La_2Mo_2O_9$ at room temperature is monoclinic [43] with a unit cell volume of 8799.554 Å [3], whereas upon doping the unit cell size decreases drastically. Due to lattice size shrinkage, the grain

size may decrease. Furthermore, the non-significant variation in lattice parameters is also related to isovalent substitution.

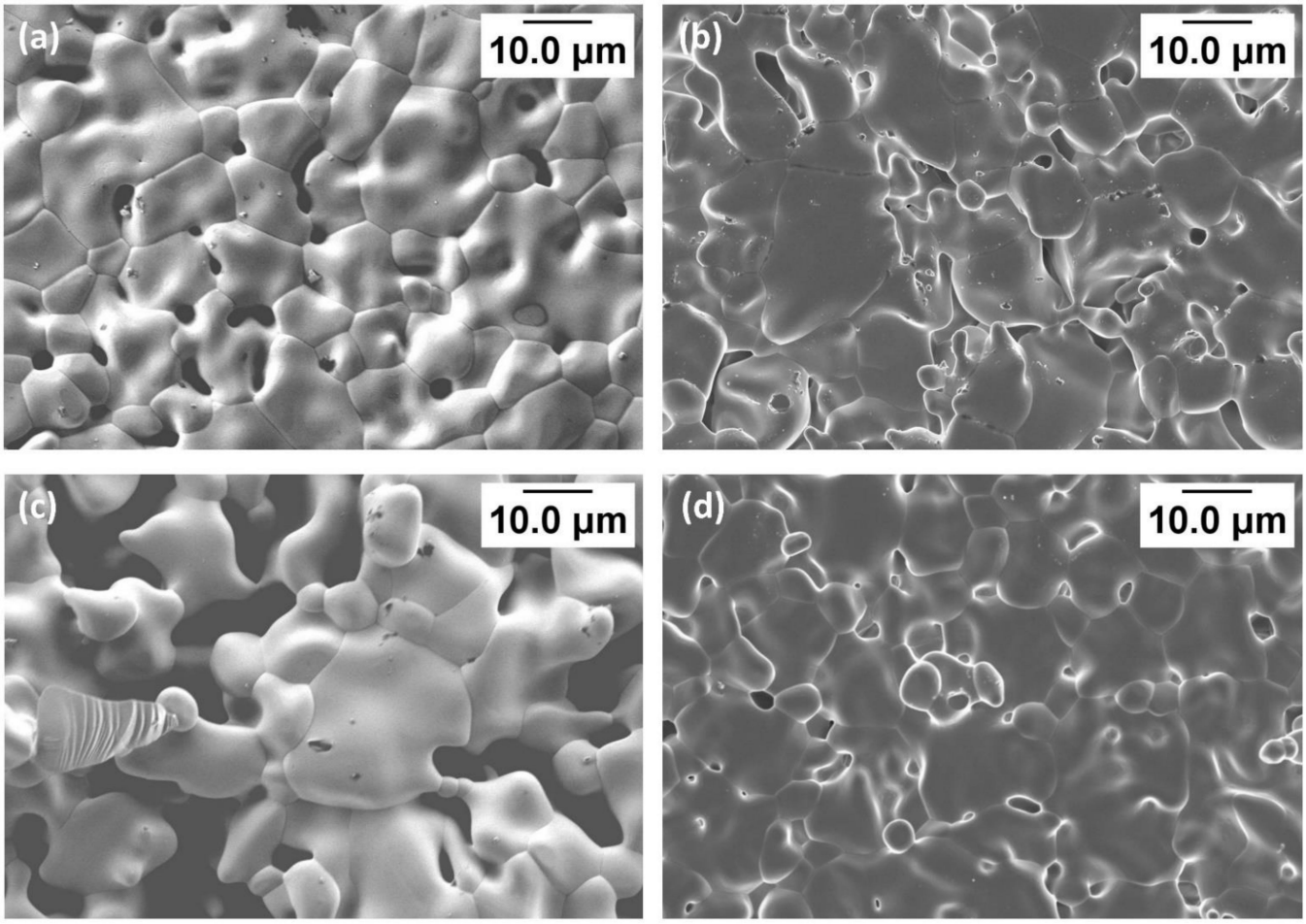

Figure 4. SEM micrographs for (**a**) 0.5 W; (**b**) 1.0 W; (**c**) 1.25 W and (**d**) 1.5 W with grain and grain boundaries.

3.4. Impedance Spectroscopy

The complex impedance plots (Nyquist plots) show strong temperature and composition dependence (Figure 5 and Figures S5–S8). The impedance spectra contain at least one complete arc at all temperatures, whereas an incomplete arc is observed at low temperatures (up to 400 °C). A typical distinction of grain, grain boundary and electrode polarization effects is performed by ISGP. For example, Figure 6, relative to the 0.5 W sample, shows that at 375 °C, a spike-like extension corresponds to the electrode process, while the two semicircles correspond to grain and grain boundaries. At 475 °C, the semicircle corresponding to the grains dissipates with the ohmic contribution, and only the grain boundary and electrode contributions are visible. Similar behavior is also observed at 575 °C. This complex variation due to substitution, as well as temperature, is difficult to model by conventional equivalent circuit modeling. ISGP, however, finds 4 peaks, considering the whole frequency spectra.

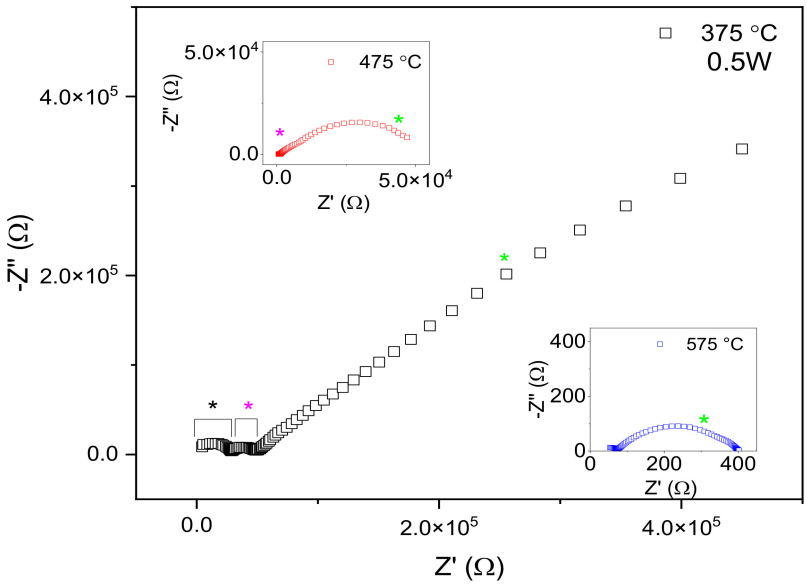

Figure 5. Nyquist plot at different temperatures for 0.5 W sample. *: bulk; *: grain boundary and *: electrode effect.

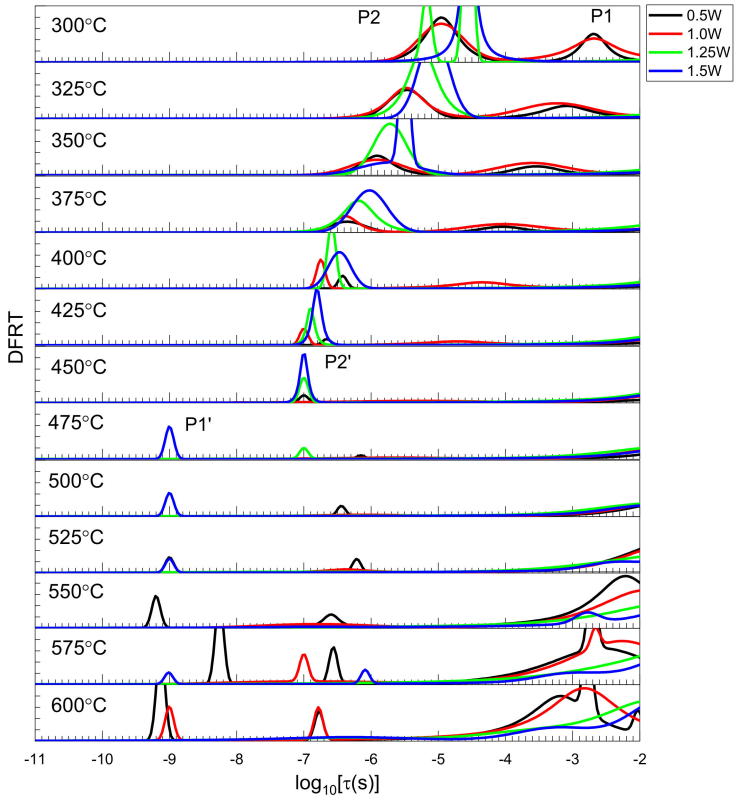

Figure 6. DFRT plots at different temperatures and compositions. Some peak heights are truncated for better visualization.

To understand the evolution and physical properties of the peaks, the area of each peak is computed. Multiplying the area by the normalization factor (typically, the real part of the impedance at the lowest frequency), and dividing by the total area, produces the relevant effective resistance (R_{eff}), and the division of the central peak position by this R_{eff} determines the effective capacitance (C_{eff}). As observed in Figure 6, all the samples at high temperatures contain the contribution of the ohmic drop. This originates because of the

non-completeness of the impedance arcs (see Figures S5–S8). The low-frequency peaks, which originate from the dispersion of the Pt electrode at the sample interface, are shown in Figures 6 and 7. Meanwhile, peaks P1 and P2 are visible up to 425 °C (Figure 6) for 0.5 W and 1.0 W. The C_{eff}'s, as calculated for P1 and P2, correspond to 10^{-11} F and 10^{-9} F, and justify the effect of grain and grain boundaries, respectively. As the temperature increases, the contribution of grain superposes with the series resistances and corresponds to P1′, with $C_{eff} \sim 10^{-12}$ F. Typically, series resistance is a resistance between two electrodes, and a blank space between the origin (0, 0) and the starting point of the real part of the impedance is considered as series resistance, as observed in the Nyquist plot (see the inset of Figure 5). It can be seen that peak P2 does not show a regular shift, as observed from 300 °C; instead, it shows a range of frequency starting from 450 °C. Henceforth, this is marked as P2′. Thus, peak P2′ depends on temperature, composition and frequency. The peak P2′ has $C_{eff} \sim 10^{-9}$ F, exhibiting the effect of grain boundaries for all the samples. Overall, the peaks P1, P2, P1′ and P2′ correspond to grain, grain boundaries, a contribution of the grain that superposes with the series resistances, and an effect of grain boundaries at different time scales, respectively. The effect of grain bulk is not visible for both 1.25 W and 1.5 W. Previously, for W-doped samples up to 1.4 W ($La_2Mo_{2-x}W_xO_9$, x = 1.4), the oxide ion conductivity showed a deviation from linearity around 450 °C, and such behavior has been explained with VTF type motion (mobility that is thermally assisted by the environment) [28]. In VTF type motion, the conductivity follows Equation (2):

$$\sigma(T) = (\sigma_0/T)\, exp((-B)/(k(T - T_0))) \quad (2)$$

where T_0 is the transition temperature of ion mobility, B is the pseudo-activation energy, k is the Boltzmann constant and σ_0 is the pre-exponential factor. In the VTF process, a vibration in the local environment of a mobile ion is observed, which is high enough to move the ion above the temperature T_0 [28]. At present, we have detected such anomaly using DFRTs as seen in Figure 6 around 450 °C. Thus, a change in ionic motion is detectable using DFRTs. More specifically, the DFRTs contain peaks that are localized on particular time-constants (τ_p) where $\tau_p = R_{eff} \cdot C_{eff}$, and each electrochemical phenomenon can be identified by the τ_p's. Thus, a shift in peak position is caused by the external factor (here, temperature). Since the Arrhenius to Vogel–Tammann–Fulcher transition is a thermally activated process, such a transition is identified by the peak shifts, as described above. Although the high-temperature XRD suggests there is no structural phase transition, the ion transport studies indicate a transition around 450 °C, which is further evident by the reciprocal temperature dependence plot of resistances and conductivities (Figures 8 and S9). Specifically, the Arrhenius to VTF transitions are observed for 0.5 W and 1.0 W from 425 °C, considering the grain-related peak, for 1.25 W from 475 °C, considering the grain boundary-related peak, and for 1.5 W from 425 °C, considering the grain boundary-related peak.

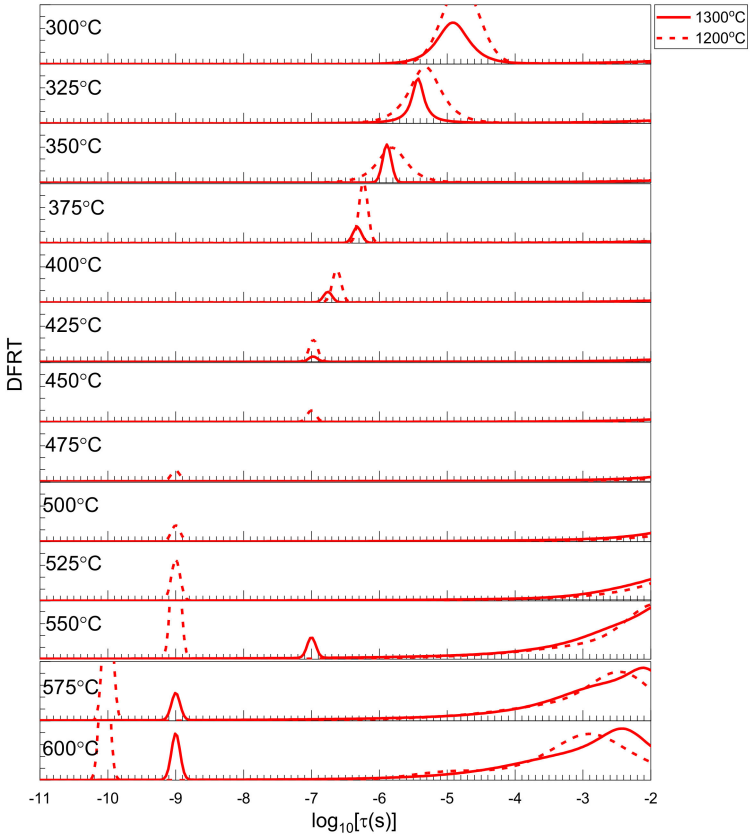

Figure 7. DFRT plots as obtained after heat treatments of the 1.0 W pellets. Some peak heights are truncated for better visualization. The peaks obtained from 525–600 °C and above 1.0 MHz for both heat-treatment samples correspond to the ohmic contribution.

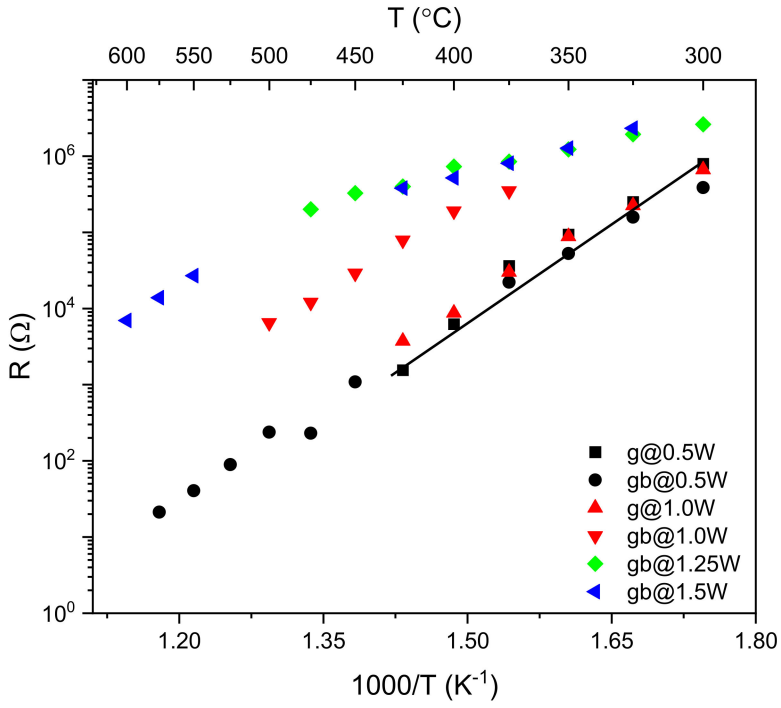

Figure 8. Reciprocal temperature dependence of resistances for P1 and P2 peaks for all the compositions. The solid line is the linear least-square fit. The fitting to other compositions are omitted for clarity. "g": grain and "gb": grain boundary.

The incorporation reaction suggests that the W substitution does not produce extra oxygen vacancies, as shown using the Kröger–Vink notation:

$$La_2O_3 + WO_3 + MoO_3 \overset{La_2Mo_2O_9}{\rightarrow} 2La_{La}^{\times} + Mo_{Mo}^{\times} + W_{Mo}^{\times} + 9O_O^{\times} \quad (3)$$

where $W_{Mo}^{\times}$ represents doping defects. Thus, here, the oxide ion conductivity is due to an intrinsic oxygen vacancy originating from the partially vacant oxygen sites, and the anomaly (Arrhenius to VTF transition) around 450 °C is due to anti-tetrahedral distortion [28].

It can be seen that the grain-size distribution is not uniform (Figure S4) for 1.25 W and 1.5 W, and the neck region can be observed between bigger grains (Figure 4c,d). The special arrangement of grains suppresses the grain contribution, as compared to grain boundaries. This explains why the grain contribution is not observed in the DFRTs for 1.25 W and 1.5 W (Figure 6). Secondly, the grain-boundary diffusion predominates, as the activation energies decrease abruptly (Table 3). LAMOX members show an activation energy of ~1.2 eV (see Table 3 and [28,44]). Low-activation energy (0.37 eV) is reported for $La_{1.9}Y_{0.1}Mo_2O_9$ in a reduced atmosphere, exhibiting electronic transport [45]. Here, the low-activation energy corresponds to the electronic contribution of the grain boundary. Nevertheless, the electronic contribution of grain boundaries is also reported when using DFRTs in $La_2Mo_{2-x}Ta_xO_9$ ($0.02 \leq x \leq 0.10$) [37] and $Ce_{0.90}Gd_{0.10}O_{1.95}$ [38] oxide ion conductors. More specifically, electronic transport refers to electron conduction, unlike ionic conduction in oxide ion conductors, whereas the electronic contribution in grain boundaries refers to the space charge layer effect for oxide ion conductors [38].

Table 3. Activation energies for the ionic process from both grain (E_g) and grain boundary (E_{gb}) for different compositions, as calculated from resistances and conductivity plots from the Arrhenius regime only. The error value is described in parenthesis. '-' represents undetermined values.

Composition	From Resistance Plot (Figure 8)		From Conductivity Plot (Figure S8)	
(x)	(E_g) (eV)	(E_{gb}) (eV)	(E_g) (eV)	(E_{gb}) (eV)
0	1.03 (±0.05)	1.22 (±0.01)	1.03 (±0.05)	1.22 (±0.01)
0.5	1.68 (±0.05)	1.53 (±0.05)	1.68 (±0.05)	1.53 (±0.05)
1.0	1.41 (±0.02)	1.43 (±0.03)	1.41 (±0.05)	1.43 (±0.05)
1.25	-	0.53 (±0.12)	-	0.53 (±0.10)
1.50	-	0.65 (±0.06)	-	0.65 (±0.06)

To find the effect of thermal treatment on ionic conductivity, we carried out additional impedance measurements on a 1.0 W sample, heated again at 1300 °C and 1200 °C, separately, for 6 h after sintering at 1100 °C. As can be seen in Figure 7, the DFRTs show a similar feature as that found in Figure 6. No shift in peak position justifies that the effects of grain, grain boundaries, and ohmic drop are independent of external factors (such as heat treatments) and depend only on the crystal structure.

The reciprocal temperature dependence of the individual resistances obtained from grain and grain boundaries indicates their semiconducting property, as shown in Figures 8 and S9. To get an estimation of the activation energy (E), the data have been modeled using the Nernst–Einstein equation [46].

$$\sigma(T) = A_0 e^{-\frac{E}{kT}} \quad (4)$$

where A_0 is the pre-exponential factor. The grain and grain boundary conductivities are related to the resistances, with $\sigma_g = \frac{l}{R_g A}$ and $\sigma_{gb} = \frac{l}{R_{gb} A}$, respectively. l is the thickness and A is the area of the pellets. The total conductivity is obtained using the relation from [18], $\sigma = l/\left(R_g + R_{gb}\right)A$. The total conductivity is found to be a maximum of 0.5 W, as is also

noted by others [18]. For instance, at 575 °C, 0.5 W, as prepared by us, possesses a total conductivity of 0.011 S cm^{-1}, which is greater than that reported by [19] (0.007 S cm^{-1}). Furthermore, the oxide ion conductivity of 0.5 W is greater than $Zr_{0.84}Y_{0.16}O_{1.92}$ at 575 °C (0.004 S cm^{-1}) [19]. As can be seen from the table, the activation energies for both grain and grain boundaries decrease with increasing W content. However, they remain in the range of 1.4–1.7 eV, which is also in accordance with the values reported by Georges et al. [28]. Since both the grain and grain boundary resistances increase in spite of the decrement of *E*'s, it can be inferred that the pre-exponential factor in Equation (4) plays a major role [28]. A similar conclusion can be drawn from the conductivity plot (Figure S9) and Table 3.

Other studies by [18,19] deal with structure, thermal and electrical properties of W-substituted samples for the potential application of these materials in SOFCs. However, we have found a couple of interesting features regarding the fundamental understanding of oxide ion conductivity. For instance, we have shown that a transition in the thermal expansion curve is both temperature- and composition-dependent. Secondly, we have analyzed the impedance data using a model-free approach (without using circuits with series/parallel combinations of resistors/capacitors) called ISGP. ISGP computes the distribution function of relaxation times and identifies the effect of ohmic, grain, and grain boundaries. As shown in the supporting figures (Figures S5–S8), the impedance spectra contain complicated patterns that could not be fitted with the same combination (model) of Rs and Cs using circuit modeling. In addition, we have determined the true capacitances using the ISGP program instead of an ad hoc representation of constant phase elements (opportune combinations in series or parallel of resistors and capacitors).

4. Conclusions

$La_2Mo_{2-x}W_xO_9$ ($0.5 \leq x \leq 1.5$) ceramic samples with a cubic structure were prepared by a solid-state synthesis method with a two-step process. The substitution with W suppressed the structural phase transition, as confirmed by both low-angle and high-resolution XRD measurements at different temperatures. The lattice parameter shows a non-linear behavior with the increasing W content. An anomaly not related to a structural phase transition is detected in the dilatometric curves for W-substituted samples. The addition of W does not show a strong variation in grain size, as confirmed by the scanning electron microscopy results. The distribution function of relaxation times, complemented by ISGP, identifies the contribution of grain and grain boundaries. Our approach identifies ohmic loss processes without extrapolating the impedance data at high frequencies and high temperatures. The grain contribution in oxide ion conductivity has not been identified for 1.25 W samples and a higher content of W. With increasing W substitution, the activation energy decreases for both grain and grain boundaries.

Supplementary Materials: The following are available online at https://www.mdpi.com/article/10.3390/ceramics4030037/s1, Table S1. The room-temperature X-ray diffraction Rietveld refinement agreement factors for different samples. The unit cell parameters and cell volume are also shown. Figure S1: Typical validation of the Kramers–Krönig relationship is shown for 0.5 W at 600 °C. The solid line represents the data obtained by the KK relationship. Figure S2: Room-temperature XRD pattern of α-$La_2Mo_2O_9$. Three Bragg peaks, as detected from the slow scan, are shown in the inset. (b) and (c) are Rietveld refinement patterns of $La_2Mo_2O_9$, considering the cubic and monoclinic phases, respectively. The refinement agreement factors in Table S1 suggest that the room-temperature pattern of $La_2Mo_2O_9$ is monoclinic (α phase). Figure S3: The depth of the pores is shown in SEM images of (a) and (b) for 1.25 W and (c) and (d) for 1.5 W. In (a) and (b), the image contrasts are shown by changing from secondary to in-lens detectors, respectively. The same experiment is also performed in (c) and (d) to identify the "real" porosity of the samples. Figure S4: Histograms for evaluating the average grain size and the distribution of grain sizes for 0.5 W, 1.0 W, 1.25 W and 1.5 W. Figure S5: Nyquist plot of impedances at different temperatures for 0.5 W. Figure S6: Nyquist plot of impedances at different temperatures for 1.0 W. Figure S7: Nyquist plot of impedances at different temperatures for 1.25 W. Figure S8: Nyquist plot of impedances at different temperatures

for 1.5 W. Figure S9. Reciprocal temperature dependence of grain and grain boundary conductivities. "g": grain and "gb": grain boundary. The linear least-squares fits are not shown for better clarity.

Author Contributions: Conceptualization, T.P. and Y.T.; methodology, T.P.; software, Y.T.; validation, T.P.; formal analysis, T.P.; resources, Y.T.; writing—original draft preparation, T.P.; writing—review and editing, T.P. and Y.T.; visualization, T.P.; supervision, Y.T.; project administration, Y.T.; funding acquisition, Y.T. All authors have read and agreed to the published version of the manuscript.

Funding: This research was partly funded by the Planning & Budgeting Committee, Israel Council for Higher Education, in the frame of the Israel National Research Center for Electrochemical Propulsion (INREP) and the Israeli Ministry of Energy. T.P. wishes to thank the Lady Davis Fellowship.

Data Availability Statement: The data presented in this study are available on request from the corresponding author.

Conflicts of Interest: The authors declare no conflict of interest. The funders had no role in the design of the study; in the collection, analyses, or interpretation of data; in the writing of the manuscript, or in the decision to publish the results.

References

1. Lacorre, P.; Goutenoire, F.; Bohnke, O.; Retoux, R.; Laligant, Y. Designing Fast Oxide-Ion Conductors Based on $La_2Mo_2O_9$. *Nature* **2000**, *404*, 856–858. [CrossRef]
2. Vega-Castillo, J.E.; Ravella, U.K.; Corbel, G.; Lacorre, P.; Caneiro, A. Thermodynamic Stability of $La_2Mo_{2-y}W_yO_9$, $La_2Mo_{2-y}W_yO_{8.96+0.02y}$ and $La_7Mo_{7(2-y)/2}W_{7y/2}O_{30}$ (y = 0, 0.5). *Dalton Trans.* **2014**, *43*, 2661–2669. [CrossRef]
3. Sellemi, H.; Coste, S.; Ben, A.; Retoux, R.; Samia, L.; Lacorre, P. Synthesis of $La_2Mo_2O_9$ Powders with Nanodomains Using Polyol Procedure. *Ceram. Int.* **2013**, *39*, 8853–8859. [CrossRef]
4. Malavasi, L.; Fisher, C.A.; Islam, M.S. Oxide-Ion and Proton Conducting Electrolyte Materials for Clean Energy Applications: Structural and Mechanistic Features. *Chem. Soc. Rev.* **2010**, *39*, 4370–4387. [CrossRef] [PubMed]
5. Georges, S.; Goutenoire, F.; Laligant, Y.; Lacorre, P. Reducibility of Fast Oxide-Ion Conductors $La_{2-x}RxMo_{2-y}W_yO_9$ (R = Nd, Gd). *J. Mater. Chem.* **2003**, *13*, 2317. [CrossRef]
6. Paul, T.; Ghosh, A. Ionic Conductivity and Dielectric Relaxation in Y Doped $La_2Mo_2O_9$ Oxide-Ion Conductors. *J. Appl. Phys.* **2014**, *116*, 144102. [CrossRef]
7. Paul, T.; Tsur, Y. Data for New Protocol to Detect the Monoclinic Phase of $La_2Mo_2O_9$ and Related Oxide Ion Conductors. *Data Br.* **2018**, *18*, 1637–1641. [CrossRef]
8. Basu, S.; Sujatha Devi, P.; Maiti, H.S.; Lee, Y.; Hanson, J.C. Lanthanum Molybdenum Oxide: Low-Temperature Synthesis and Characterization. *J. Mater. Res.* **2006**, *21*, 1133–1140. [CrossRef]
9. Basu, S.; Devi, P.S.; Maiti, H.S.; Bandyopadhyay, N.R. Synthesis, Thermal and Electrical Analysis of Alkaline Earth Doped Lanthanum Molybdate. *Solid State Ion.* **2013**, *231*, 87–93. [CrossRef]
10. Paul, T.; Ghosh, A. Conduction and Relaxation Mechanisms in Bismuth Doped $La_2Mo_2O_9$ Ionic Conductors. *J. Appl. Phys.* **2013**, *114*, 164101. [CrossRef]
11. Paul, T.; Ghosh, A. Correlation of Structure and Ion Conduction in $La_{2-x}Y_xMo_2O_9$ ($0 \leq x \leq 0.2$) Oxygen Ion Conductors. *J. Appl. Phys.* **2015**, *117*, 235101. [CrossRef]
12. Basu, S.; Sujatha Devi, P.; Bandyopadhyay, N.R. Sintering and Densification Behavior of Pure and Alkaline Earth (Ba^{2+}, Sr^{2+} and Ca^{2+}) Substituted $La_2Mo_2O_9$. *J. Eur. Ceram. Soc.* **2013**, *33*, 79–85. [CrossRef]
13. Selmi, A.; Corbel, G.; Kojikian, S.; Voronkova, V.; Kharitonova, E.; Lacorre, P. Complex Effect of Partial Substitution of La^{3+} by Ca^{2+} on the Stability of Fast Oxide-Ion Conductor $La_2Mo_2O_9$. *Eur. J. Inorg. Chem.* **2008**, *2008*, 1813–1821. [CrossRef]
14. Marozau, I.; Marrero-López, D.; Shaula, A.L.; Kharton, V.; Tsipis, E.; Núñez, P.; Frade, J. Ionic and Electronic Transport in Stabilized β-$La_2Mo_2O_9$ Electrolytes. *Electrochim. Acta* **2004**, *49*, 3517–3524. [CrossRef]
15. Corbel, G.; Durand, P.; Lacorre, P.; Cedex, L.M. Comprehensive survey of Nd^{3+} substitution in $La_2Mo_2O_9$ oxide-ion conductor. *J. Solid State Chem.* **2009**, *182*, 1009–1016. [CrossRef]
16. Pavlova, S.; Bespalko, Y.; Krieger, T.; Sadykov, V.; Uvarov, N. Genesis, Structural, and Transport Properties of $La_2Mo_{2-x}W_xO_9$ Prepared via Mechanochemical Activation. *Ionics* **2016**, *23*, 877–887. [CrossRef]
17. Voronkova, V.I.; Yanovski, V.K.; Kharitonova, E.P. Oxygen-Conducting Crystals of $La_2Mo_2O_9$: Growth and Main Properties. *Crystallogr. Rep.* **2005**, *50*, 874–876. [CrossRef]
18. Marrero-López, D.; Canales-Vázquez, J.; Ruiz-Morales, J.C.; Irvine, J.T.S.; Núñez, P. Electrical Conductivity and Redox Stability of $La_2Mo_{2-x}W_xO_9$ Materials. *Electrochim. Acta* **2005**, *50*, 4385–4395. [CrossRef]
19. Marrero-López, D.; Peña-Martínez, J.; Ruiz-Morales, J.C.; Pérez-Coll, D.; Martín-Sedeño, M.C.; Núñez, P. Applicability of $La_2Mo_{2-y}W_yO_9$ Materials as Solid Electrolyte for SOFCs. *Solid State Ion.* **2007**, *178*, 1366–1378. [CrossRef]
20. Corbel, G.; Laligant, Y.; Goutenoire, F.; Suard, E.; Lacorre, P. Effects of Partial Substitution of Mo^{6+} by Cr^{6+} and W^{6+} on the Crystal Structure of the Fast Oxide-Ion Conductor Structural Effects of W^{6+}. *Chem. Mater.* **2005**, *17*, 4678–4684. [CrossRef]

21. Kong, X.-S.; Hou, C.J.; Hao, Q.-H.; Liu, C.S.; Wang, X.P.; Fang, Q.F. First Principle Study of Structural, Phase Stabilization and Oxygen-Ion Diffusion Properties of β-$La_{2-x}L_xMo_2O_9$ (L = Gd, Sm, Nd and Bi) and β-$La_2Mo_{2-y}M_yO_9$ (M = Cr, W). *Solid State Ion.* **2009**, *180*, 946–951. [CrossRef]
22. Marrero-López, D.; Canales-Vázquez, J.; Zhou, W.; Irvine, J.T.S.; Núñez, P. Structural Studies on W^{6+} and Nd^{3+} Substituted $La_2Mo_2O_9$ Materials. *J. Solid State Chem.* **2006**, *179*, 278–288. [CrossRef]
23. Ruan, B.; Yan, B.; Zhang, J. Effect of Oxygen Partial Pressure on the Electrical Conductivity of $La_2Mo_{2-x}W_xO_{9-\delta}$ (x = 0.0, 0.5, 0.7) Materials. *Solid State Sci.* **2012**, *14*, 840–848. [CrossRef]
24. Siddharth; Bysakh, S.; Sil, A. X-ray Photoelectron Spectroscopy and Ion Dynamics Study of W^{6+} Doped $La_2Mo_2O_9$ as SOFC Electrolyte. *Mater. Res. Bull.* **2018**, *105*, 36–44. [CrossRef]
25. Jin, T.Y.; Madhava Rao, M.V.; Cheng, C.L.; Tsai, D.S.; Hung, M.H. Structural Stability and Ion Conductivity of the Dy and W Substituted $La_2Mo_2O_9$. *Solid State Ion.* **2007**, *178*, 367–374. [CrossRef]
26. Pandey, R.; Singh, S.; Singh, P. Modified Polyol-Mediated Synthesis of Sr- and W-Substituted $La_2Mo_2O_9$ Solid Electrolyte for Solid Oxide Fuel Cells. *J. Mater. Sci. Mater. Electron.* **2020**, *31*, 11325–11335. [CrossRef]
27. Tian, C.; Shao, L.; Ji, D.; Yang, J.; Xie, J.; Yin, Q.; Le, H. Synthesis and Characterization of Tungsten and Barium Co-Doped $La_2Mo_2O_9$ by Sol-Gel Process for Solid Oxide Fuel Cells. *J. Rare Earths* **2019**, *37*, 984–988. [CrossRef]
28. Georges, S.; Bohnke, O.; Goutenoire, F.; Laligant, Y.; Fouletier, J.; Lacorre, P. Effects of Tungsten Substitution on the Transport Properties and Mechanism of Fast Oxide-Ion Conduction in $La_2Mo_2O_9$. *Solid State Ion.* **2006**, *177*, 1715–1720. [CrossRef]
29. Rodríguez-Carvajal, J. Recent Advances in Magnetic Structure Determination by Neutron Powder Diffraction. *Phys. B Condens. Matter* **1993**, *192*, 55–69. [CrossRef]
30. Borenstein, A.; Hershkovitz, S.; Oz, A.; Luski, S.; Tsur, Y.; Aurbach, D. Use of 1,10-Phenanthroline as an Additive for High-Performance Supercapacitors. *J. Phys. Chem. C* **2015**, *119*, 12165–12173. [CrossRef]
31. Susai, F.A.; Talianker, M.; Liu, J.; Paul, T.; Grinblat, Y.; Erickson, E.; Noked, M.; Burstein, L.; Frenkel, A.I.; Tsur, Y.; et al. Electrochemical Activation of Li_2MnO_3 Electrodes at 0 °C and Its Impact on the Subsequent Performance at Higher Temperatures. *Materials* **2020**, *13*, 4388. [CrossRef]
32. Mishuk, E.; Ushakov, A.; Makagon, E.; Cohen, S.R.; Wachtel, E.; Paul, T.; Tsur, Y.; Shur, V.Y.; Kholkin, A.; Lubomirsky, I. Electro-chemomechanical Contribution to Mechanical Actuation in Gd-Doped Ceria Membranes. *Adv. Mater. Interfaces* **2019**, *6*, 1801592. [CrossRef]
33. Tesler, A.B.; Lewin, D.R.; Baltianski, S.; Tsur, Y. Analyzing Results of Impedance Spectroscopy Using Novel Evolutionary Programming Techniques. *J. Electroceram.* **2010**, *24*, 245–260. [CrossRef]
34. Hershkovitz, S.; Tomer, S.; Baltianski, S.; Tsur, Y. ISGP: Impedance Spectroscopy Analysis Using Evolutionary Programming Procedure. In Proceedings of the ECS Transactions, Las Vegas, NV, USA, 10–15 October 2010; Volume 33. [CrossRef]
35. Baltianski, S.; Tsur, Y. Analysis of Impedance Spectroscopy Data—Finding the Best System Function. *J. Electroceram.* **2003**, *10*, 89–94. [CrossRef]
36. Su, K.H.; Chi, P.W.; Paul, T.; Chung, C.H.; Chen, W.M.; Su, Y.S.; Wu, P.M.; Su, C.Y.; Wu, M.K. Lithiation and Delithiation Induced Magnetic Switching and Electrochemical Studies in α-$LiFeO_2$ Based Li Ion Battery. *Mater. Today Phys.* **2021**, *18*, 100373. [CrossRef]
37. Paul, T.; Ghosh, A. Structure and Electrical Conductivity of Ta Doped $La_2Mo_2O_9$ Oxide Ion Conductors. *J. Appl. Phys.* **2018**, *124*, 225102. [CrossRef]
38. Paul, T.; Yavo, N.; Lubomirsky, I.; Tsur, Y. Determination of Grain Boundary Conductivity Using Distribution Function of Relaxation Times (DFRT) Analysis at Room Temperature in 10 Mol% Gd Doped Ceria: A Non-Classical Electrostrictor. *Solid State Ion.* **2019**, *331*, 18–21. [CrossRef]
39. Paul, T.; Tsur, Y. Effect of Isovalent Doping on Grain Boundary Conductivity for $La_2Mo_2O_9$ Oxide Ion Conductor: A Distribution Function of Relaxation Times Approach. *Solid State Ion.* **2018**, *323*, 37–43. [CrossRef]
40. Shannon, R.D. Revised Effective Ionic Radii and Systematic Studies of Interatomie Distances in Halides and Chaleogenides. *Acta Crystallogr.* **1976**, *32*, 751. [CrossRef]
41. Subramania, A.; Saradha, T.; Muzhumathi, S. Synthesis and Characterization of Nanocrystalline $La_2Mo_2O_9$ Fast Oxide-Ion Conductor by an in-Situ Polymerization Method. *Mater. Res. Bull.* **2008**, *43*, 1153–1159. [CrossRef]
42. Natoli, A.; Arias-Serrano, B.I.; Rodríguez-Castellón, E.; Żurawska, A.; Frade, J.R.; Yaremchenko, A.A. Mixed Ionic-Electronic Conductivity, Redox Behavior and Thermochemical Expansion of Mn-Substituted 5ysz as an Interlayer Material for Reversible Solid Oxide Cells. *Materials* **2021**, *14*, 641. [CrossRef] [PubMed]
43. Evans, I.R.; Howard, J.A.K.; Evans, J.S.O. The Crystal Structure of R-$La_2Mo_2O_9$ and the Structural Origin of the Oxide Ion Migration Pathway. *Chem. Mater.* **2005**, *17*, 4074–4077. [CrossRef]
44. Sen, S.; Paul, T. Electronic Structures of Trivalent Cations Doped Bulk and Cubic $La_2Mo_2O_9$ Oxide Ion Conductors. *J. Solid State Chem.* **2021**, *295*, 121918. [CrossRef]
45. Pinet, P.; Fouletier, J.; Georges, S. Conductivity of Reduced $La_2Mo_2O_9$ Based Oxides: The Effect of Tungsten Substitution. *Mater. Res. Bull.* **2007**, *42*, 935–942. [CrossRef]
46. Shewmon, P. (Ed.) *Diffusion in Solids*; Springer: Berlin/Heidelberg, Germany, 2016. [CrossRef]